arXiv:1410.2307v1 [cond-mat.mtrl-sci] 8 Oct 2014

Epitaxial growth of $Bi_2Pt_2O_7$ pyrochlore

Araceli Gutiérrez–Llorente*,[1,*] Howie Joress,[2,3] Arthur Woll,[2] Megan E. Holtz,[1]
Matthew J. Ward,[2] Matthew C. Sullivan,[4] David A.Muller,[1] and Joel D. Brock[1,2]

[1] *Cornell University, School of Applied and Engineering Physics, Ithaca, New York, 14853, USA*
[2] *Cornell University, Cornell High Energy Synchrotron Source, Ithaca, New York, 14853, USA*
[3] *Cornell University, Department of Materials Science and Engineering, Ithaca, New York, 14853, USA*
[4] *Ithaca College, Department of Physics and Astronomy, Ithaca, New York, 14850, USA*

(Dated: March 3, 2022)

Certain pyrochlore oxides[1] are among the best oxygen catalysts in alkaline media.[2–9] Hence, exploring epitaxial films of these materials is of great fundamental and technological interest. Unfortunately, direct film growth of one of the most promising pyrochlores, $Bi_2Pt_2O_7$,[10] has not yet been achieved, owing to the difficulty of oxidizing platinum metal in the precursor material to Pt^{4+}. In this work, in order to induce oxidation of the platinum, we annealed pulsed laser deposited films consisting of epitaxial δ–Bi_2O_3 and co–deposited, comparatively disordered platinum. We present synchrotron x–ray diffraction results that show the annealed films are the first epitaxial crystals of $Bi_2Pt_2O_7$. We also visualized the pyrochlore structure by scanning transmission electron microscopy, and observed ordered cation vacancies in a bismuth–rich film but not in a platinum–rich film. The similarity between the δ–Bi_2O_3 and $Bi_2Pt_2O_7$ structures appears to facilitate the pyrochlore formation. These results constitute a new approach for synthesis of novel pyrochlore thin film oxygen catalysts.

Pyrochlore oxides, $A_2B_2O_7$,[4] that exhibit catalytic activity are prospective cathode materials for fuel cells. Furthermore, the oxygen ion conductivity of some pyrochlores is comparable to that of oxides with fluorite structure, such as yttria–stabilized zirconia.[3,6,7] In this regard, one of the most promising pyrochlores for catalytic applications is bismuth platinum oxide, $Bi_2Pt_2O_7$. Previous work on powders of $Bi_2Pt_2O_7$ found its electrochemical activity essentially identical to pure Pt.[10] Furthermore, compared to bulk powders, enhanced catalytic activity has been observed in epitaxially grown perovskite oxides and structural derivatives.[11–14] These results have contributed to growing interest in epitaxial films of pyrochlore oxides as an oxygen catalyst. However, while nanocrystalline powders of $Bi_2Pt_2O_7$ by thermal oxidation of Bi–Pt nanoparticles has been reported,[15] epitaxial crystals of $Bi_2Pt_2O_7$ have not yet been achieved.

Here we report the first, successful formation of epitaxial $Bi_2Pt_2O_7$ (111) on YSZ(111) single–crystal substrates. Our synthesis strategy consists of a deposition step followed by a post-growth anneal. During growth, epitaxial Bi_2O_3 is formed in its cubic δ phase, while co-deposited platinum forms an as-yet undetermined state, exhibiting only minute amounts of metallic platinum in specular x–ray diffraction (XRD). Annealing in air transforms the δ–Bi_2O_3 into epitaxial crystals of $Bi_2Pt_2O_7$ pyrochlore.

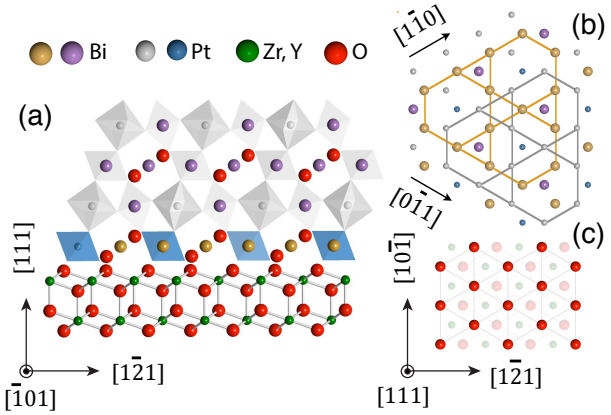


FIG. 1: **Structural model of $Bi_2Pt_2O_7$(111)/YSZ(111).** **a**, View along [$\bar{1}$01]. The pyrochlore structure consists of corner–linked PtO_6 distorted octahedra (the oxygen atoms at their vertices are omitted for clarity) with the Bi atoms filling the interstices. YSZ(111), modeled with a fluorite lattice, is composed of oxygen–metal–oxygen triple layers. **b**, Kagome arrangements of Bi atoms (Bi, dark yellow; Pt, blue) alternate with kagome patterns of Pt atoms (Bi, purple; Pt, gray) along [111]. (Bi–Bi or Pt–Pt bonds are guides to the eye). **c**, YSZ(111) surface is oxygen terminated (predicted as the most stable one).[17] The topmost oxygen ions form an hexagonal array.

Fig.1 displays the side (a), and top (b, c) views of the structural model of $Bi_2Pt_2O_7$(111)/YSZ(111). $Bi_2Pt_2O_7$ has a lattice parameter approximately twice that of YSZ, but consists of eight nearly identical fluorite subunits with intrinsic oxygen vacancies on 1/8 of the oxygen sites. The misfit between these subunits and the YSZ substrate is 0.8% (from our results, a_s=5.147 Å, for YSZ; and, a_f=10.371 Å for $Bi_2Pt_2O_7$ in bulk[16] form).

We studied the out–of–plane orientation of the films by XRD. Fig.2 (a) shows θ– 2θ scans of an as–deposited film (blue pattern). The growth was carried out at an oxygen pressure of 10^{-4} Torr, a substrate temperature of 640° C, and a laser fluence of 3 J/cm^2. The as–

grown pattern reveals intense peaks that can be assigned to (111), (222) and (333) (not shown) cubic δ–Bi_2O_3. Distinct thickness fringes are observed surrounding the (111) Bragg peak of δ–Bi_2O_3 in the as–grown films (Supplementary Information, Fig. S1) which give evidence of a smooth film surface. Rocking curve measurements for the (111)δ–Bi_2O_3 peak (Supplementary Information, Fig. S2) show a FWHM of 0.100±0.001° in omega (rocking curve on YSZ substrates has a nominal FWHM of 0.014° in omega). The measured out–of–plane lattice parameter for δ–Bi_2O_3 is 5.519 Å, in good agreement with previous reported values.[18,19]

Although the cubic δ phase of Bi_2O_3 in bulk form is stable only from 729° C up to its melting point at 825° C and transforms to other phases upon cooling, it has previously been stabilized at room temperature on Au substrates by electrodeposition,[18] on polycrystalline YSZ substrates by atmospheric pressure chemical vapour deposition,[23] and as δ–Bi_2O_3 nanostructures on perovskite substrates.[19]

The weak diffraction peak at q=2.77 $Å^{-1}$ in Fig.2 (a, blue pattern) is consistent with that of the (111) plane of a trace amount of platinum metal with an fcc structure. Apart from the small amount of (111)–oriented platinum, these data are in agreement with several possibilities, including either amorphous platinum, $\sim$ 1 nm platinum nanocrystals that diffract similarly weakly to amorphous platinum, or platinum that is somehow incorporated into the δ–Bi_2O_3 lattice.

The phase segregation of the platinum metal and Bi_2O_3 is a major difficulty of working with this system. Like the as–deposited film, the PLD target exhibits phase separation of the platinum from the bismuth oxide. The precursor material exhibits the pyrochlore phase (Bi^{3+}, Pt^{4+}) when prepared by solid state reaction at 650°C from stoichiometric mixtures of Bi_2O_3 and platinum metal (Supplementary Information, Fig. S3). However, as expected, targets sintered at this temperature are not dense enough for proper ablation. Sintering temperatures higher than 650°C are required to synthesize high–density PLD targets, but at these temperatures Pt^{4+} reduces to platinum metal. Thus, PLD targets sintered at 820° C (slightly below the melting point of Bi_2O_3) contain platinum and Bi_2O_3 in its monoclinic α phase (Supplementary Information, Fig. S3). Consequently, platinum metal has to oxidize to Pt^{4+} so that the pyrochlore phase can form on the substrate. Furthermore, control of the Bi/Pt cation stoichiometry of the film becomes complicated due to the high volatility of the bismuth and the large difference between the melting temperatures of the two components of the target (Bi_2O_3, 825° C; Pt, 1770° C). Perovskite Bi–based films with the correct stoichiometry have been grown by PLD from bismuth–rich targets[24,25] as well as from stoichiometric targets.[26,27] There is no previous work on epitaxial films of $Bi_2Pt_2O_7$. We used *in situ* x–ray fluorescence (XRF) at grazing incidence to tune the deposition parameters while keeping track of the Bi/Pt ratio of the films. We

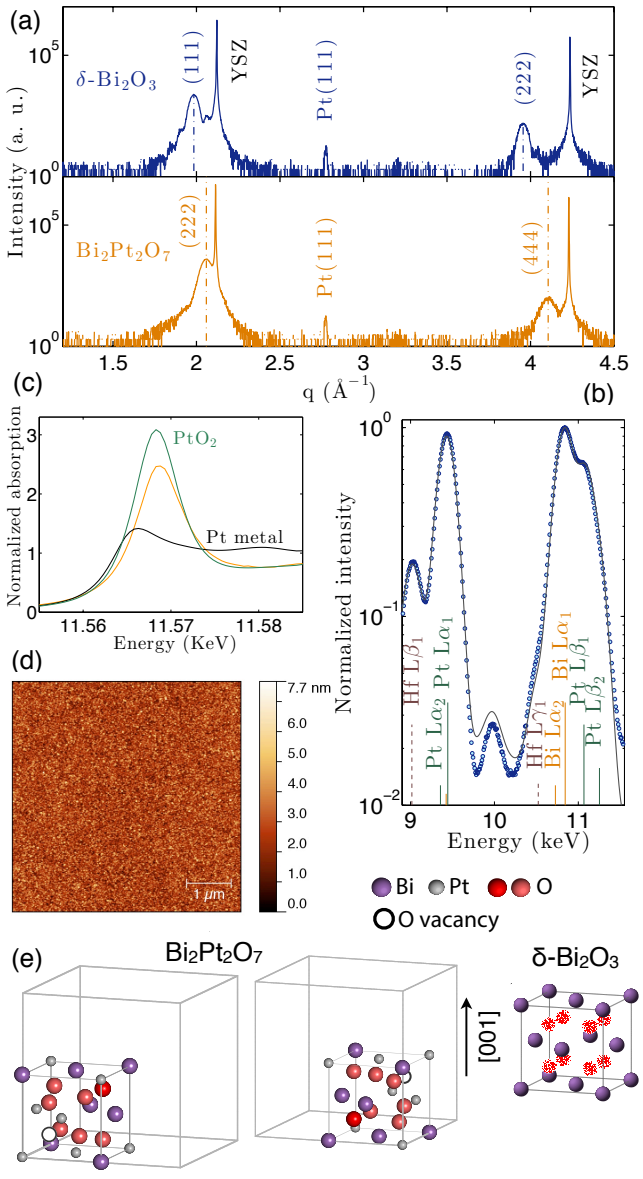


FIG. 2: **Synthesis of pyrochlore $Bi_2Pt_2O_7$. a**, XRD θ–2θ scans of a film as–grown (blue), and after post–growth anneal (orange), showing the formation of the pyrochlore phase during the anneal. **b**, Normalized grazing incidence *in situ* XRF. Bi and Pt x–ray emissions in the range 8.5 keV – 12 keV are marked with vertical lines whose heights are proportional to their relative intensity. XRF analysis shows a Bi/Pt ratio of 0.88±0.01. The Hf impurity of the YSZ substrate is also included. **c**, Pt L_3 edge XANES spectra of an annealed film (orange); and, PtO_2 (green) and Pt metal foil (black) used as reference standards. The intense peak confirms the oxidation of platinum in the annealed film. **d**, AFM image of the annealed film in panels (a) and (b). **e**, The order of Bi^{3+} and Pt^{4+} along ⟨110⟩ and that of vacancies determines two types of fluorite subcells in the pyrochlore structure. Cubic δ–Bi_2O_3 with fluorite structure where each anion site has an average occupancy of 3/4.[20–22]

chose to use a stoichiometric target, and compensate for the preferential ablation of bismuth that we observed in this system by working at a pressure of 10^{-4} Torr, lower than the bismuth vapor pressure at 640° C (bismuth vapor pressure is 10^{-4} Torr at 517° C; 10^{-2} Torr at 672° C). This leads to the sublimation of a portion of the deposited bismuth. Fig.2 (b) displays the XRF spectrum for the film shown in panel (a) measured *in situ* once the substrate temperature was cooled down. The quantitative analysis performed by a custom fitting procedure which employs the Elam database[28] provides an estimate Bi/Pt ratio of 0.88 ± 0.01 within a 95% confidence level.

In order to induce oxidation of the platinum, the film shown in Fig.2 (a, blue scan) was annealed in a tube furnace in air at 640° C for 8 h. Fig.2 (a, orange scan) displays the θ– 2θ scan of the film after annealing. This pattern shows two new peaks that can be attributed to (222) and (444) pyrochlore with an out–of–plane lattice parameter of 10.57 ± 0.02 Å. The reflections assigned in the as–grown film to {111} planes of δ–Bi_2O_3 have disappeared while the weak peak attributed to some trace of (111) platinum metal is still observable. These results support the hypothesis that the Pt(111) peak in the XRD scan of Fig.2 (a, blue pattern) cannot fully account for all the deposited platinum in the film. Rocking curve measurements for the (222)$Bi_2Pt_2O_7$ peak (Supplementary Information, Fig. S4) reveal a FWHM of 0.098±0.002° in omega, comparable to that of the (111)δ–Bi_2O_3 peak (Supplementary Information, Fig. S2).

We investigated the oxidation state of platinum in the annealed films. Fig.2(c) shows Pt L_3 edge X–ray absorption near edge structure (XANES) spectrum (orange) of a bismuth–rich annealed film (Bi/Pt=1.62±0.04) with pyrochlore phase (Supplementary Information, Fig. S5 and S6). Fig.2(c) also displays XANES spectra for a platinum metal foil (black), and PtO_2 (green) used as reference standards. The higher threshold energy (E_0) of the film in relation to that of the platinum reference foil is consistent with a higher oxidation state in the annealed film, most probably Pt^{4+}. The intense peak, referred to as white line, observed in the spectrum of the film (Fig.2(c), orange) is indicative of a metal oxide. It is thus clear that platinum oxidized during the post–growth anneal.

The smoothness of the surface of the annealed film in Fig.2(a),(b) was analyzed by atomic force microscopy (AFM). The AFM image shown in Fig.2(d) reveals a rms roughness of 0.84 nm. It was grown on a YSZ (111) stepped surface with atomically flat terraces (Supplementary Information, Fig. S7).

The structural models shown in Fig.2(e) reveal striking similarity between the cubic δ–Bi_2O_3 and the pyrochlore structures. Both are based on an ordered oxygen deficient fluorite structure. Bi^{3+} cations in δ–Bi_2O_3, as well as both Bi^{3+} and Pt^{4+} in the pyrochlore structure form an fcc lattice. This strongly suggests the stabilization of the δ phase of Bi_2O_3 is essential for the formation of the $Bi_2Pt_2O_7$ pyrochlore phase during the *ex–situ* post–growth anneal. In fact, films that contained the monoclinic (α) phase of Bi_2O_3 still exhibit α–Bi_2O_3 as the majority phase after annealing, (Supplementary Information, Fig.S8).

Remarkably, the pyrochlore phase is epitaxial. Along with high intensity peaks characteristic of the parent fluorite structure ($h+k$, $k+l$, and $l+h$ are all multiples of four), we observed weak pyrochlore superstructure peaks (their intensity is expected to be three orders of magnitude lower), such as $(33\bar{3})$ and (331).

The expected positions for the reflections of the epitaxial $Bi_2Pt_2O_7$/YSZ system are depicted in Fig.3(a). Peaks from the YSZ substrate with a fluorite lattice are also labeled. Area scans at grazing incidence around asymmetrical reflections of the $Bi_2Pt_2O_7$ phase were transformed into reciprocal space maps (RSM). They are plotted in Fig.3(b) and (c) for a bismuth–rich film and for a slightly platinum–rich film, respectively. δ–Bi_2O_3 still present in the bismuth–rich film shows up in the RSM of the $Bi_2Pt_2O_7$, revealing again the similarity between the fluorite and pyrochlore structures (Supplementary Information, Fig.S9). Superstructure peaks indicative of the pyrochlore phase are highlighted.

In–plane ($a_\parallel$) and out–of–plane ($a_\perp$) lattice constants of the epitaxial $Bi_2Pt_2O_7$, along $[0\bar{1}1]$ and [111] directions, respectively, determined from the RSMs are $a_\parallel$ = 10.46±0.03 $Å^{-1}$ and $a_\perp$=10.423±0.006 $Å^{-1}$, for the film in Fig.3(b); and, $a_\parallel$ = 10.53±0.08 $Å^{-1}$ and $a_\perp$ = 10.53±0.04 $Å^{-1}$ (in accordance, within the error, with the value obtained from the θ–2θ scan in Fig.2(a)) for the film in Fig.3(c). These figures suggest the pyrochlore is relaxed with respect to the substrate lattice.

Azimuthal ϕ scans carried out using synchrotron x–ray radiation at grazing incidence on the (200) peak of α–Bi_2O_3 of an as–grown film, Fig.3(d), and on the $(22\bar{2})$ peak of $Bi_2Pt_2O_7$ in an annealed film, Fig.3(e), confirm the epitaxial nature of the films with an in–plane orientation which gives rise to peaks with threefold symmetry. The FWHM of (200) peaks of α–Bi_2O_3 is 0.50°±0.01, and that of the $(22\bar{2})$ peaks separated 120° in the ϕ scan is 0.57°±0.02. In–plane orientation relationships of either $[10\bar{1}]$YSZ ∥ $[10\bar{1}]Bi_2Pt_2O_7$ or $[10\bar{1}]$YSZ ∥ $[1\bar{1}0]Bi_2Pt_2O_7$, rotated 60° respect to each other, can be built with the structural model shown in Fig.1(b),(c). However, no twin domains were observed in our films.

Fig.4 shows cross–sectional high–angle annular dark field (HAADF) scanning TEM images for the films whose RSMs are displayed in Fig.3(b), (c). These studies reveal ∼ 100 nm long regions of ordered epitaxial pyrochlore. A wider field of view scanning TEM images showing non–pyrochlore regions are shown in Supplementary Information, Fig.S10. Fig.4(a) exhibits the expected columns of a pyrochlore structure with cation ordered vacancies (no noticeable contrast in the HAADF is expected between Bi and Pt columns). The presence of vacancies in this case can be due to the deviation from the correct stoichiometry of the film composition, Bi/Pt=1.62±0.04. The platinum–rich film shown in Fig.3(c) with a Bi/Pt

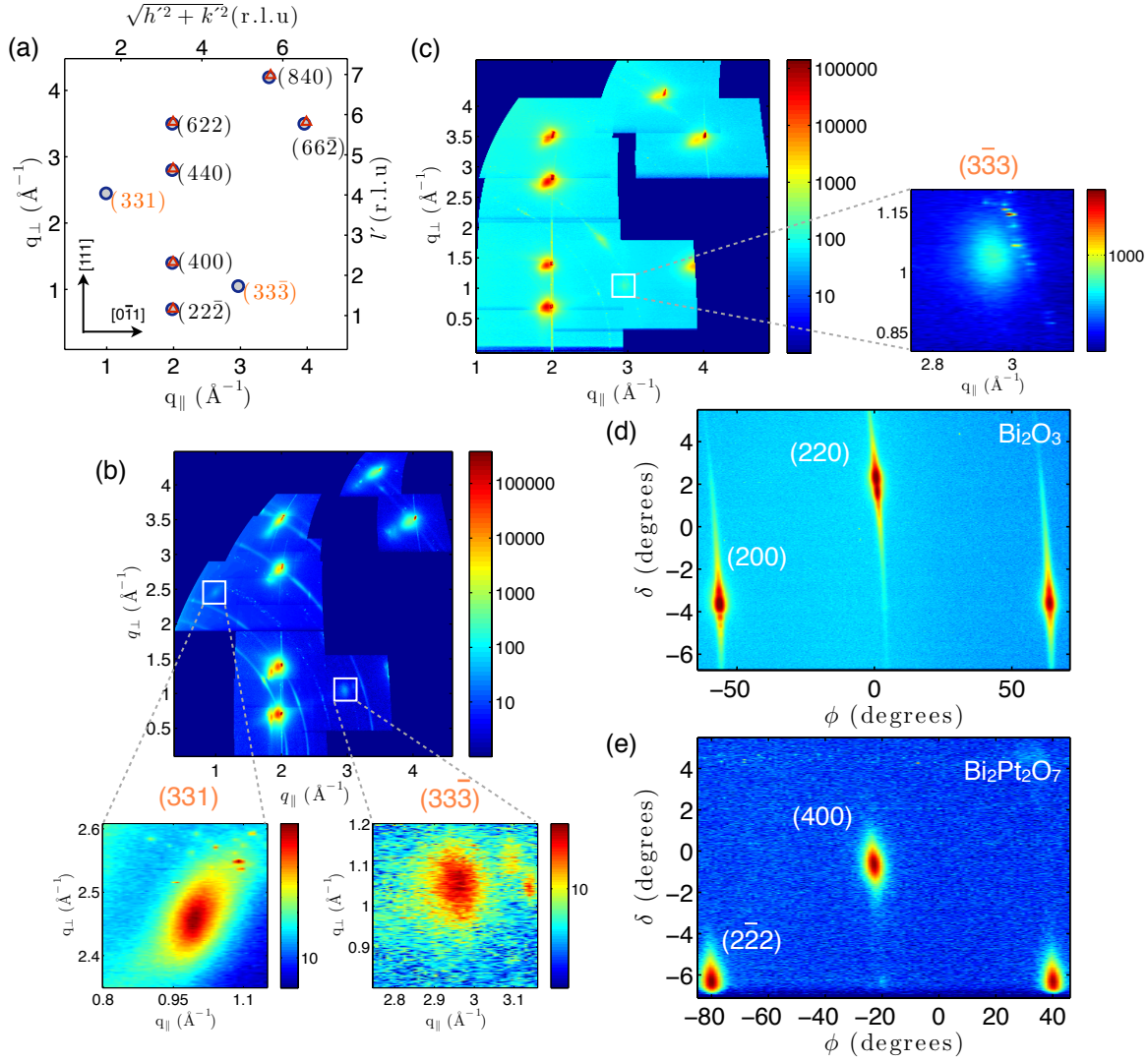


FIG. 3: **Synchrotron x–ray reciprocal space maps and ϕ–scans. a**, Calculated positions in reciprocal space for reflections of $Bi_2Pt_2O_7$ (gray filled circles), assuming the $Bi_2Pt_2O_7$ bulk lattice constant, 10.371 Å. Substrate reflections (red hollow triangles) are also expected to occur for the fluorite–like reflections of the pyrochlore lattice, where $h+k$, $k+l$, and $l+h$ are all multiples of four. h', k', l' stand for the coordinates of reciprocal vectors with respect to the set of reciprocal lattice vectors generated from $\{(\bar{1}01)/\sqrt{2}, (1\bar{2}1)/\sqrt{6}, (111)/\sqrt{3}\}$. r.l.u = reciprocal lattice units of the $Bi_2Pt_2O_7$ bulk lattice. **b, c**, Reciprocal space maps combined into a single image for a bismuth–rich film (b), and a platinum–rich film (c). The insets show an enlargement of reciprocal space for the superstructure reflections (331) and (33$\bar{3}$) of the $Bi_2Pt_2O_7$ pyrochlore phase. The intensity of all the figures is presented on a logarithmic scale. **d**, Azimuthal ϕ scan of the (200) reflection of the δ–Bi_2O_3 phase in an as–grown film, and **e**, of the (22$\bar{2}$) reflection of the $Bi_2Pt_2O_7$ phase of an annealed film. The incident angle (α) was fixed at 0.25° and 0.275°, respectively. The exit angle, $\beta = \delta - \alpha$ was collected in a range of 12°.

ratio of 0.88±0.01 does not contain cation vacancies in its pyrochlore structure, Fig.4(c).

In conclusion, these results provide a novel route for the formation of epitaxial $Bi_2Pt_2O_7$ pyrochlore, thought to be one of the most efficient oxide catalysts. Upcoming work includes the investigation of the oxygen reduction activity of the (111) surface of $Bi_2Pt_2O_7$, and its comparison with powder pellets. However, the difficulty of controlling Bi/Pt stoichiometry suggests that independent control of volatile bismuth and non–volatile platinum sources may be required for routine growth of pristine films.

* araceli.gutierrez@urjc.es; Permanent address: Universidad Rey Juan Carlos, Escuela Superior de Ciencias Experimen-

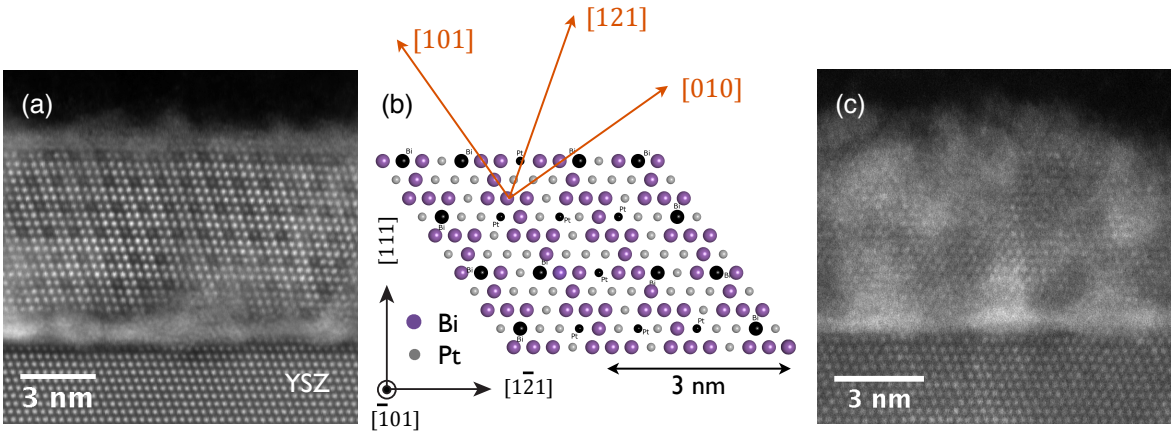


FIG. 4: **High–angle annular dark field scanning TEM images. a**, HAADF STEM image of the bismuth–rich film shown in Fig.3(b), viewed along [$\bar{1}$01] in the NION UltraSTEM. The dark, ordered atomic locations in the image are the result of cation vacancies. **b**, Schematic of the bismuth and platinum columns of the $Bi_2Pt_2O_7$ pyrochlore structure viewed along [$\bar{1}$01]. Black positions mark where the ordered cation vacancies are expected, matching the image in Fig.1(a). **c**, HAADF STEM image of the platinum–rich film shown in Fig.3(c), viewed along [$\bar{1}$01] in the Tecnai F20. Cation vacancies are not observed in this structure.

tales y Tecnología, Madrid 28933, Spain

[1] H. Horowitz, J. Longo, and J. Lewandowski, "New oxide pyrochlores: $A_2[B_{2-x}A_x]O_{7-y}$ (A : Pb, Bi; B = Ru, Ir)," Materials Research Bulletin **16**, 489–496 (1981).

[2] H. S. Horowitz, J. M. Longo, and H. H. Horowitz, "Oxygen electrocatalysis on some oxide pyrochlores," Journal of the Electrochemical Society **130**, 1851–1859 (1983).

[3] H. L. Tuller, "Mixed ionic–electronic conduction in a number of fluorite and pyrochlore compounds," Solid State Ionics **52**, 135–146 (1992).

[4] M. A. Subramanian, G. Aravamudan, and G. V. S. Rao, "Oxide pyrochlores – a review," Progress in Solid State Chemistry **15**, 55–143 (1983).

[5] P. A. Christensen, A. Hamnett, and D. Linares-Moya, "Oxygen reduction and fuel oxidation in alkaline solution," Physical Chemistry Chemical Physics **13**, 5206–5214 (2011).

[6] J. C. Boivin and G. Mairesse, "Recent material developments in fast oxide ion conductors," Chemistry of materials **10**, 2870–2888 (1998).

[7] B. J. Wuensch, K. W. Eberman, C. Heremans, E. M. Ku, P. Onnerud, E. M. Yeo, S. M. Haile, J. K. Stalick, and J. D. Jorgensen, "Connection between oxygen-ion conductivity of pyrochlore fuel-cell materials and structural change with composition and temperature," Solid State Ionics **129**, 111–133 (2000).

[8] A. Kahoul, P. Nkeng, A. Hammouche, F. Nâmoune, and G. Poillerat, "A sol–gel route for the synthesis of $Bi_2Ru_2O_7$ pyrochlore oxide for oxygen reaction in alkaline medium," Journal of Solid State Chemistry **161**, 379–384 (2001).

[9] T. Konishi, H. Kawai, M. Saito, J. Kuwano, H. Shiroishi, T. Okumura, and Y. Uchimoto, "Electrocatalytic activity of the pyrochlores $Ln_2M_2O_{7-\delta}$ (Ln = Lanthanoids) for oxygen reduction reaction," Topics in Catalysis **52**, 896–902 (2009).

[10] N. K. Beck, B. Steiger, G. G. Scherer, and A. Wokaun, "Methanol tolerant oxygen reduction catalysts derived from electrochemically pre–treated $Bi_2Pt_{2\pm y}Ir_yO_7$ pyrochlores," Fuel Cells **6**, 26–30 (2006).

[11] G. J. la O, S. J. Ahn, E. Crumlin, Y. Orikasa, M. D. Biegalski, H. M. Christen, and Y. Shao-Horn, "Catalytic activity enhancement for oxygen reduction on epitaxial perovskite thin films for solid-oxide fuel cells," Angewandte Chemie-International Edition **49**, 5344–5347 (2010).

[12] J. Liu, G. Collins, M. Liu, C. Chen, J. He, J. Jiang, and E. I. Meletis, "Ultrafast oxygen exchange kinetics on highly epitaxial $PrBaCo_2O_{5+\delta}$ thin films," Applied Physics Letters **100** (2012).

[13] H. Jeen, Z. Bi, W. S. Choi, M. F. Chisholm, C. A. Bridges, M. P. Paranthaman, and H. N. Lee, "Orienting oxygen vacancies for fast catalytic reaction," Advanced Materials **25**, 6459–6463 (2013).

[14] M. Kubicek, Z. Cai, W. Ma, B. Yildiz, H. Hutter, and J. Fleig, "Tensile lattice strain accelerates oxygen surface exchange and diffusion in $La_{1-x}Sr_xCoO_{3-\delta}$ thin films," ACS Nano **7**, 3276–3286 (2013).

[15] F. Dawood, B. M. Leonard, and R. E. Schaak, "Oxidative transformation of intermetallic nanoparticles: An alternative pathway to metal/oxide nanocomposites, textured ceramics, and nanocrystalline multimetal oxides," Chemistry of Materials **19**, 4545–4550 (2007).

[16] E. Beck and S. Kemmlersack, "The semiconductor-metal transition in bismuth pyrochlores of the system $Bi_2Pt_{2-y}Ir_yO_7$," Journal of the Less–Common Metals **135**, 257–268 (1987).

[17] G. Ballabio, M. Bernasconi, F. Pietrucci, and S. Serra, "Ab initio study of yttria–stabilized cubic zirconia surfaces," Physical Review B **70**, 075417 (2004).

[18] J. Switzer, M. G. Shumsky, and E. Bohannan, "Electrodeposited ceramic single crystals," Science **5412**, 293–296 (1999).

[19] D. L. Proffit, G.-R. Bai, D. D. Fong, T. T. Fister, S. O. Hruszkewycz, M. J. Highland, P. M. Baldo, P. H. Fuoss, T. O. Mason, and J. A. Eastman, "Phase stabilization

of δ–Bi_2O_3 nanostructures by epitaxial growth onto single crystal $SrTiO_3$ or $DyScO_3$ substrates," Applied Physics Letters **96**, 021905 (2010).

[20] P. D. Battle, C. R. A. Catlow, J. W. Heap, and L. M. Moroney, "Structural and dynamic studies of δ–Bi_2O_3 oxide ion conductors," Journal of Solid State Chemistry **63**, 8–15 (1986).

[21] M. Yashima and D. Ishimura, "Crystal structure and disorder of the fast oxide-ion conductor cubic Bi_2O_3," Chemical Physics Letters **378**, 395–399 (2003).

[22] C. E. Mohn, S. Stolen, S. T. Norberg, and S. Hull, "Oxide–ion disorder within the high temperature δ phase of Bi_2O_3," Physical Review Letters **102** (2009).

[23] T. Takeyama, N. Takahashib, T. Nakamurab, and S. Itoh, "δ–Bi_2O_3 thin films deposited on dense YSZ substrates by CVD method under atmospheric pressure for intermediate temperature SOFC applications," Surface & Coatings Technology **200**, 4797–4801 (2006).

[24] S. Havelia, S. Wang, M. Skowronski, and P. A. Salvador, "Controlling the Bi content, phase formation, and epitaxial nature of $BiMnO_3$ thin films fabricated using conventional pulsed laser deposition, hybrid pulsed laser deposition, and solid state epitaxy," Journal of Applied Physics **112** (2009).

[25] V. Shelke, V. N. Harshan, S. Kotru, and A. Gupta, "Effect of kinetic growth parameters on leakage current and ferroelectric behavior of $BiFeO_3$ thin films," Journal of Applied Physics **106** (2009).

[26] L. You, N. T. Chu, K. Yao, L. Chen, and J. Wang, "Influence of oxygen pressure on the ferroelectric properties of epitaxial $BiFeO_3$ thin films by pulsed laser deposition," Physical Review B **80** (2009).

[27] Y. Kim, A. Morozovska, E. Eliseev, M. P. Oxley, R. Mishra, S. M. Selbach, T. Grande, S. T. Pantelides, S. V. Kalinin, and A. Y. Borisevich, "Direct observation of ferroelectric field effect and vacancy–controlled screening at the $BiFeO_3/La_xSr_{1-x}MnO_3$ interface," Nature Materials **13**, 879–883 (2014).

[28] W. Elam, B. Ravel, and J. Sieber, "A new atomic database for x–ray spectroscopic calculations," Radiation Physics and Chemistry **63**, 121–128 (2002).

[29] B. Ravel and M. Newville, "ATHENA, ARTEMIS, HEPHAESTUS: data analysis for X–ray absorption spectroscopy using IFEFFIT," Journal of Synchrotron Radiation **12**, 537–541 (2005).

Methods

We sintered the PLD target from a mixture of Bi_2O_3 (99.999%) and Pt powder ($\leq$20 μm, $\geq$99.97%) with controlled cation stoichiometry (Bi/Pt=1) in a solid–state reaction. These mixtures were ground in an agate mortar, pressed into pellets, and heated in a box furnace at 800°C for 3 h. Then, the pellets were ground and sintered again at 650°C for 48 h. This annealing at 650°C for 48 h was repeated five times, with intermediate grinding and pressing. In order to get high-density PLD targets, the powders were reground and repressed, and then fired at 820°C for further 24 h. X–ray diffraction patterns (Rigaku SmartLab, Cu source) were taken on the intermediate pellets and on the final targets. Their cation stoichiometry was measured by x–ray fluorescence. Polished cross-sections of the targets were studied by high resolution scanning electron microscopy and energy dispersive X–ray spectroscopy (LEO 1550 Field Emission SEM).

Films were grown in the *in situ* PLD system housed at the G3 hutch of Cornell High Energy Synchrotron Source (CHESS's) which utilizes a KrF excimer laser (248 nm) focused onto the target. During the growth, oxygen was supplied in the PLD chamber yielding a background pressure up to 10^{-1} Torr. The substrate temperature, monitored by an optical pyrometer (λ = 4.8–5.3 μm, ϵ = 0.8) and a thermocouple, was set in the range 450 °C – 740 °C. Single-crystals 8 mol % Y_2O_3–stabilized ZrO_2 ($(ZrO_2)_{0.92}$ $(Y_2O_3)_{0.08}$), YSZ) with (111) orientation (MTI Corporation) were used as substrates. Prior to the growth, they were annealed at 1300° C for 3 h in air. Atomic Force Microscopy (AFM, Veeco Dimension 3100 system) on the annealed substrates showed steps of height ∼0.3 nm corresponding to the distance of successive {111} planes (oxygen–metal–oxygen triple layer) separated by terraces.

The Bi and Pt content of the films were monitored *in situ* by X-ray fluorescence (XRF) at grazing incidence. The excitation energy was 13.64 keV (synchrotron radiation), above the Bi L_3 absorption edge (13.42 keV). L_α x–ray emission lines of Bi (L_{α_1} at 10.84 KeV) and Pt (L_{α_1} at 9.44 KeV) were used to quantify the Bi/Pt ratio. The quantitative analysis of the XRF spectrum was performed by a custom fitting procedure implemented in MATLAB which employs the Elam database.[28] The model provides an estimate of the Bi/Pt ratio by fitting a calculated spectrum to the measured one.

Ex situ XRD $\theta/2\theta$ scans were performed in a four–circle diffractometer (Rigaku SmartLab, Cu source, Ge(220) 2–bounce incident beam monochromator). X–ray diffraction under grazing incidence experiments were conducted at CHESS G2 hutch with an incident energy of 10.04 keV or 13.64 keV. The incidence angle was set to 0.25° or 0.275°. Area scans around the asymmetrical reflections of the film were transformed to reciprocal space maps (RSM) and combined into a single figure. In–plane and out–of–plane lattice parameters were determined from RSMs.

X–ray absorption near edge structure (XANES) measurements at the Pt L_3 edge (11.564 keV) were carried out at the F3 beamline of CHESS. A silicon (220) double-crystal monochromator with an energy resolution ΔE/E of $\approx 10^{-4}$ was used. A Pt reference foil standard, used for energy calibration, was measured in transmission mode downstream of the sample between two ion chambers filled with 100% N_2. All XANES data were calibrated and normalized using the Demeter Athena XAS software package.[29]

Cross-sectional TEM specimens were investigated in the 5th–order aberration corrected 100 keV NION UltraSTEM with a probe size of 1 Å for a bismuth-rich sample, and the monochromated 200 keV FEI Tecnai F-20 STEM/TEM with a probe size of 1.6 Å for a platinum-rich sample. The specimens were prepared using the FEI Strata 400 focused ion beam, with a final ion milling with 2 keV gallium ions to minimize surface damage. HAADF-STEM imaging was used in both machines, which offers atomic resolution atomic number contrast, going roughly as the square of the atomic number, with heavier atoms appearing brighter.

Acknowledgements

We acknowledge Hanjong Paik for helpful discussions; Darrrel Schlom for making available the equipment in his laboratory to prepare YSZ substrates; Raymond Burns and Frank DiSalvo for providing us an initial amount of pyrochlore powder to start this work.

This work is based upon research conducted at the Cornell High Energy Synchrotron Source (CHESS) which is supported by the National Science Foundation and the National Institutes of Health/National Institute of General Medical Sciences under NSF awards DMR-0936384 and DMR-1332208. This work also made use of the Cornell Center for Materials Research Shared Facilities that are supported through the NSF MRSEC program (DMR-1120296).

A.G.L acknowledges financial support from the Spanish Ministry of Education, Culture and Sport under research grant PRX12/00405; the CajaMadrid Foundation (Spain) under a re-

search grant, 2012 call; and, the Energy Materials Center at Cornell (emc^2), an Energy Frontier Research Center funded by the U.S. Department of Energy, Office of Science, Office of Basic Energy Sciences under award number DE-SC0001086.

Author contributions

A.G.L. designed the experiments and led this research project; synthesized and characterized the targets, prepared and characterized the YSZ substrates, and grew the films; performed the *ex situ* XRD θ–2θ scans, the *in situ* XRF, and the AFM measurements; analyzed the XRD (θ–2θ), reciprocal space maps and XRF data; prepared the figures and wrote the manuscript. M.C.S., H.J. and A.G.L. tune the PLD system up. A.W. and A.G.L. performed area scans for asymmetrical reflections at G2 (CHESS). A.W. wrote the MATLAB code to transform area scans carried out at G2 (CHESS) into RSMs, and to combine several RSMs into a single figure, and began XRF studies at G3 for this system on silicon substrates. M.E.H. and D.A.M. performed STEM studies. M.C.S. assisted in preliminary growths of films consisting of Bi_2O_3 ant Pt phases. M.J.W. prepared the PtO_2 standard for XANES measurements. M.J.W. and H.J. measured XANES at Pt L_3 edge (F3 beamline, CHESS). J.D.B. made available the resources and equipments of his group to develop this research. All the authors discussed the manuscript.

Additional information

Supplementary information is available.

Competing financial interests

The authors declare no competing financial interests.